Comparison of Simulated and Measured Flux Distributions at the Aperture of the Next-CSP Solar Receiver

Benjamin Grange[1, a)], Antoine Perez[1], William Baltus[1], Alex Le Gal[1] and Gilles Flamant[1]

[1]PROMES-CNRS, 7 rue du Four Solaire, 66120 Font-Romeu-Odeillo-Via, France.

[a)]benjamin.grange@promes.cnrs.fr

Abstract. In the framework of the Next-CSP project that aims at demonstrating a fluidized particles-in-tube solar receiver concept at pilot scale, a thorough control of the heat flux distribution on the tubes is compulsory to avoid appearance of hot spots likely leading to receiver damage. The control of the heat flux distribution is carried out by an aiming point strategy on the receiver tubes and validated by comparing simulated and experimental flux distribution at the aperture of the solar receiver by using a scanning bar. The simulated and experimental solar flux distributions at the receiver aperture plane are compared for a single heliostat focusing at the aperture of the Themis tower.

INTRODUCTION

The Next-CSP project aims at installing and testing a fluidized particles-in-tube solar receiver concept at pilot scale. The solar receiver is made of 40 tubes of 3 meters height surrounded by a half cavity made of three refractory panels, as shown in Fig. 1. The angles of the cavity panels comes from position of most Eastern, Western and Northern heliostats.

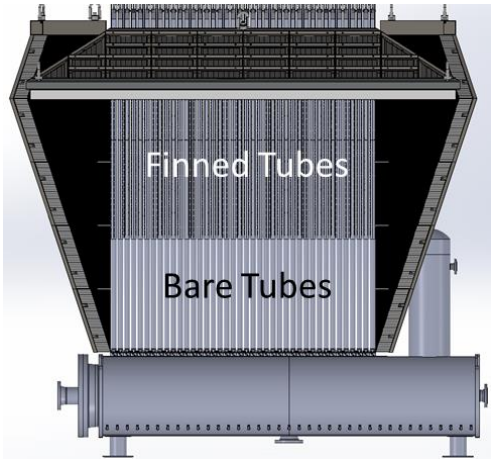

FIGURE 1. 3D model of the solar receiver with the cavity

A refractory panel is also installed behind the tubes to reflect the concentrated radiation passing through the gaps between the tubes. To preserve the lifetime of the receiver and ensure a uniform particle outlet temperature in each tube, the control of the flux distribution through an aiming point strategy on the receiver is essential. To make sure

that the simulated and experimental flux distributions are similar, a scanning bar is installed and travels in front of the receiver cavity. This paper first describes the methodology of the aiming point strategy relying on the TABU search associated with a convolution-projection model and a ray-tracing software. Then the post-treatment to build the experimental flux distribution with the scanning plate is detailed. Finally, the simulated and experimental flux distributions at the scanning plate's plane for a single heliostat are compared.

AIMING POINT STRATEGY

Aiming point strategy (APS) is investigated by applying the meta-heuristic method [1] associated with the convolution-projection optical model UNIZAR [2]. The APS is carried out on an aperture plane located on the mid-plane of the tubes. A 3 m x 3 m aperture plane is considered and 25 points are defined.
An objective normalized flux distribution is defined and located at the mid-plane of the tubes, with a limitation in the maximum flux density of 500 kW/m². After reaching the optimized results, taking into account a constraint on the spillage loss (not more than 30% of the intercepted power in the reference case), the aiming points are introduced into the ray-tracing software *Solstice* [3] that computes the flux distribution on the receiver tubes.

Figure 2 shows a typical result of the flux distribution on the receiver tubes applying the APS.

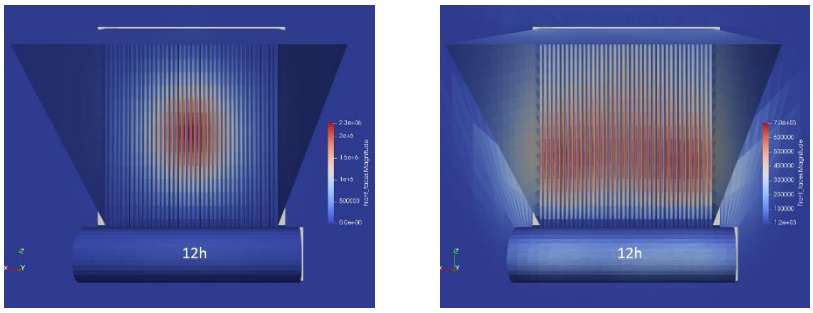

FIGURE 2. Flux distribution on the receiver tubes before (right) and after (left) applying the APS

A virtual target is positioned at the aperture of the solar receiver cavity, on the same plane where the scanning bar travels. Figure 3 shows the simulated flux distribution at the scanning bar's plane.

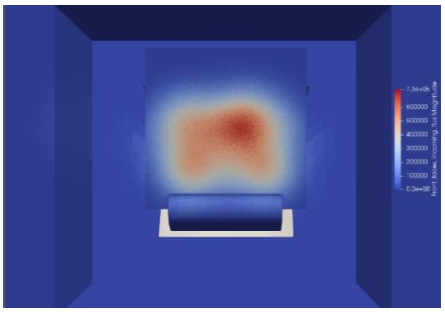

FIGURE 3. Flux distribution on a virtual target located at the scanning plate's plane

This simulated flux distribution on the virtual target must be compared with the experimental flux distribution reconstructed after the travel of the scanning bar. The experimental set-up and the data processing to reconstruct the flux distribution are explained in the following section.

MEASUREMENT OF THE FLUX DISTRIBUTION

Experimental Set-Up

The heat flux measurement system consists in a Basler CMOS camera offering a high picture frame rate (up to 163 fps), a high resolution (1920x1200 pixels) and a high dynamic (16-bit). The camera is equipped with a 300 mm lens. Figure 4 shows the camera that is located in a shelter in the center of the solar field and the view of the aperture from the camera. The distance between the camera and the aperture of the solar receiver is 120 meters.

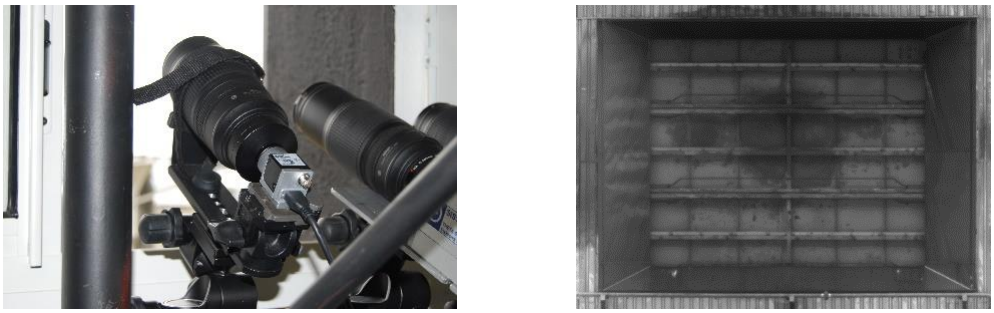

FIGURE 4. CMOS camera installed in a shelter in the center of the solar field (left) and view of the aperture with the camera (right)

It records pictures of a scanning bar (shown in Fig. 5) that travels from East/West to West/East in front of the aperture of the receiver cavity at a velocity of 2 m/s. The scanning bar has a black band on each side to create contrast in the bright pictures. An algorithm using a spatial derivative approach results in the reconstruction of the intensity distribution.

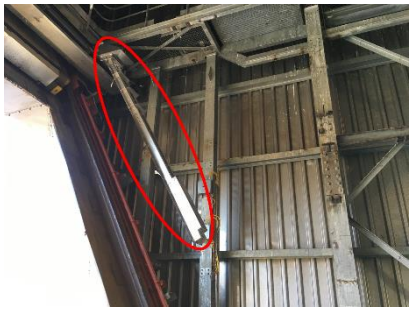

FIGURE 5. Picture of the scanning bar (surrounded in red) installed at the receiver aperture before installation of the solar loop

Finally, a fast response heat flux micro-sensor (HFM 6 from Vatell) integrated in this bar calibrates the intensity distribution into a flux distribution. It is a 4 mm in diameter thermopile covered with Pyromark film and offering a 17 to 300 μs response time. The accuracy claimed by the supplier is ± 3%. A high-speed A/D converter and a data acquisition system (ADDI DATA MSX-E3011) are also installed on the scanning bar in order to avoid noise in the micro-signal delivered by the heat flux sensor (Fig. 6).

FIGURE 6. Picture of the heat flux micro-sensor, converter and acquisition integrated in the scanning bar

Figure 7 shows pictures taken from the heliostat field of the scanning bar travel. A metallic shield is installed behind to block the concentrated radiation and protect the components inside the tower.

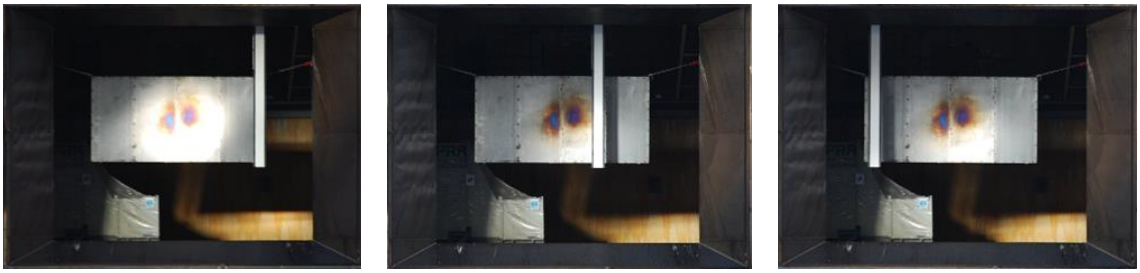

FIGURE 7. Pictures taken from the heliostat field of during the travel of the scanning bar

Data Processing

The data processing follows the method presented by A. Ferrière et al. [4].

Flat-Field Correction

The data processing starts with a flat field correction that aims at eliminating or reducing measurement noise and bias. To carry out this process, the lens on the camera is first covered with a tap while the camera settings are unchanged: same area of interest on the CCD matrix, same gain and shutter speed. A sequence of 1000 images is taken and the median average is computed. A black image is obtained and named I_{black}. The black image contains the electronic bias and noise generated by the A/D converter. Then the tap is replaced by a uniform brightness source and the same sequence is repeated. A flat-field image is obtained and named I_{flat}. This flat-field image contains the noise and distortion generated by each pixel when discharging their current and the optical defaults resulting from dust or scratches possibly remaining on the lens. Each raw image I_{raw} of the sequence taken during the scanning is converted into a "net" image I_{net} using the following equation:

$$I_{net} = \frac{I_{raw} - I_{black}}{I_{flat} - I_{black}} \quad (1)$$

The Peak Signal to Noise Ratio (PSNR) can be calculated for each image by applying:

$$PSNR = 10log_{10}\left(\frac{1}{rms(I_{raw} - I_{net})}\right) \quad (2)$$

Where $rms(I_{raw} - I_{net})$ is the root mean square deviation between the raw and the net image. A PSNR value above 40 guarantees that the noise and bias are correctly removed.

Detection of the Bar

A background image I_{back} is taken at the end of the bar's travel and is subtracted from each net image, resulting in a final sequence called "corrected" image I_{corr}:

$$I_{corr} = I_{net} - I_{back} \tag{3}$$

This operation allows increasing the contrast between the bar and the surrounding. Then the derivative between two neighboring pixels on a horizontal line in a same corrected image is calculated. A big change in brightness occurs due to the two black bands, thus offering a better detection of the bar.

The corrected images are normalized using the maximum and the minimum values of each pixel in all the sequence:

$$I_{corr-n} = 2\frac{I_{corr} - Min_{pix-all}}{Max_{pix-all} - Min_{pix-all}} - 1 \tag{4}$$

The gradient along the horizontal axis is then calculated:

$$I_{grad-x} = grad_x(I_{corr-n}) \tag{5}$$

The gradient is normalized using the maximum and the minimum values of gradient in all the sequence:

$$I_{grad-x-n} = 2\frac{I_{grad-x} - Min_{grad-x-all}}{Max_{grad-x-all} - Min_{grad-x-all}} - 1 \tag{6}$$

Finally, the average value of the normalized gradient is calculated along each column:

$$Mean_{grad-x-n} = mean_y\left(I_{grad-x-n}\right) \tag{7}$$

The result of this approach is shown in Fig. 8 where a margin of error is introduced to reject the black bands and to eliminate any deviation due to the shadow of the bar projected on the background.

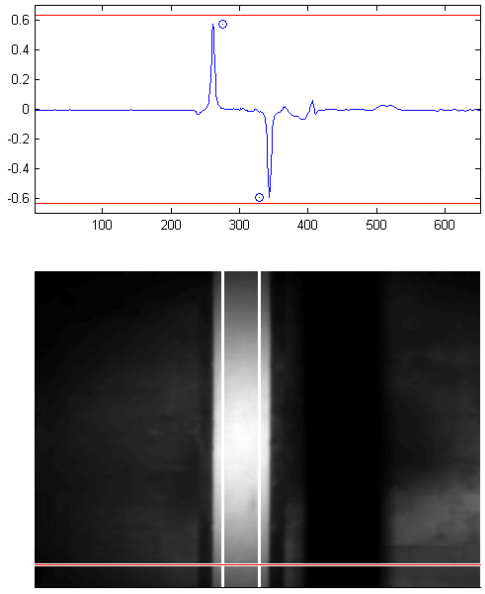

FIGURE 8. Detection of the bar using the normalized gradient averaged per column (top) and the application of margin of error (bottom)

Mapping the Grey Value

The *n* values available for pixel *p* are entered in a vector $ValPixel_p(n)$. The mean value of this vector is calculated:

$$MeanValPixel(p) = \frac{1}{n}\sum_{i=1}^{n} ValPixel_p(i) \quad (8)$$

The standard deviation *STD(p)* is also calculated:

$$STD(p) = \frac{1}{n}\sqrt{\sum_{i=1}^{n}\left[ValPixel_p(i) - MeanValPixel(p)\right]^2} \quad (9)$$

Finally the pixel value in the map *ValPixel(p)* is the average of the value fulfilling the following condition (the other one being rejected):

$$MeanValPixel(p) - 2 \times STD(p) < ValPixel_p(i) < MeanValPixel(p) + 2 \times STD(p) \quad (10)$$

The complete map in grey scale is obtained by applying this approach for each pixel.

Calibration

The calibration is carried out by matching the measured flux with the intensity profile on the horizontal line where the heat flux micro-sensor travels, as shown in Fig. 9. A mean value of the ratio *FluxDensity/ValPixel(x)* is calculated and allows converting the intensity distribution into a flux distribution.

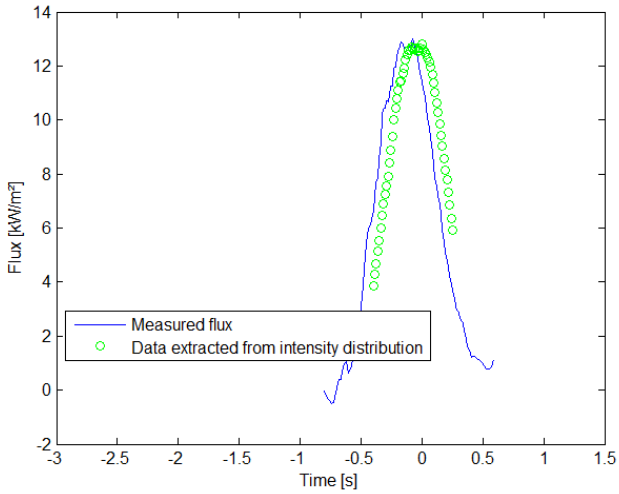

FIGURE 9. Time series $F_{measured}$ (in solid line blue) and *ValPixel* (in green dots)

RESULTS

Figure 10 shows the simulated and experimental flux distribution given by a single heliostat at the aperture of the receiver. The slope error is set to 1.7 mrad.

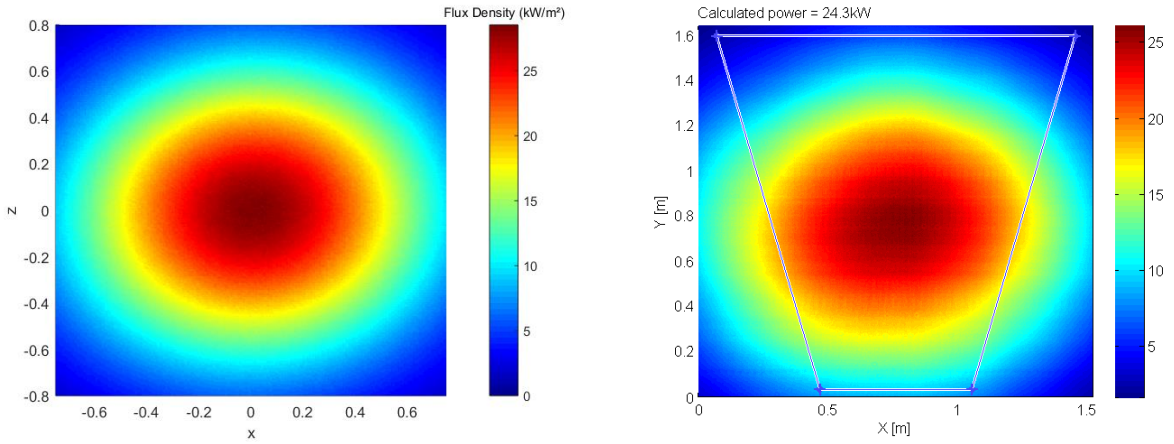

FIGURE 10. Comparison between simulated (left) and experimental (right) flux distribution

The shape of the heliostat focal spot is very similar between the simulation and the measurement. The higher flux density observed in the simulated flux distribution is likely due to some dust on the heliostat mirrors decreasing their reflectance.

DISCUSSION AND PERSPECTIVES

First results with a single heliostat are encouraging. However further comparisons with more heliostats and with an aiming point strategy must be performed in order to validate the theoretical flux distribution at the aperture of the solar receiver. This will be achieved when operating the solar receiver.

ACKNOWLEDGMENTS

This project has received funding from the European Union's Horizon 2020 research and innovation program under grant agreement No 727762, project acronym NEXT-CSP.

This work was supported by the French "Investments for the future" program managed by the National Agency for Research, under contract ANR-10-EQPX-49-SOCRATE (Equipex SOCRATE).

REFERENCES

1. A. Salomé et al., Solar Energy 94, 352-366 (2014).
2. F.J. Collado et al., Journal of Solar Energy 37, 215-234 (1986).
3. PROMES-CNRS, MESO-STAR SAS. SOLSTICE, SOLar Simulation Tool In ConcEntrating optics, version 0.7.1 (2017), France, https://www.meso-star.com/projects/solstice.html https://www.labex-solstice.fr/logiciel-solstice.html.
4. A. Ferriere et al., AIP Conference Proceedings 1734, (2008) 130007.